Nanoscale

Accepted Manuscript

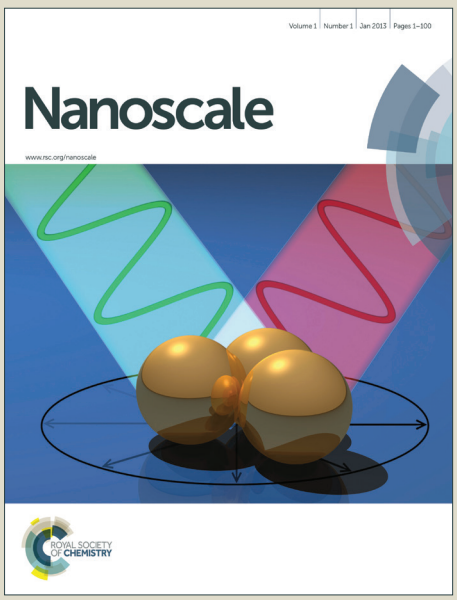

ROYAL SOCIETY OF CHEMISTRY

www.rsc.org/nanoscale

Nanoscale

RSCPublishing

ARTICLE

Cite this: DOI: 10.1039/x0xx00000x

Received ooth January 2014,
Accepted ooth January 2014

DOI: 10.1039/x0xx00000x

www.rsc.org/

Miniature all-solid-state heterostructure nanowire Li-ion batteries as a tool for engineering and structural diagnostics of nanoscale electrochemical processes

Vladimir P. Oleshko,[*a,d] Thomas Lam,[b] Dmitry Ruzmetov,[b,c] Paul Haney[b], Henri J. Lezec[b], Albert V. Davydov,[a] Sergiy Krylyuk,[a,c], John Cumings[d], and A. Alec Talin[b,e]

Complex interfacial phenomena and phase transformations that govern the operation of Li-ion batteries require detailed nanoscale 3D structural and compositional characterization that can be directly related to their capacity and electrical transport properties. For this purpose, we have designed model miniature all solid-state radial heterostructure Li-ion batteries composed of $LiCoO_2$ cathode, LiPON electrolyte and amorphous Si anode shells, which were deposited around metallized high-aspect-ratio Si nanowires as a scaffolding core. Such diagnostic batteries, the smallest, complete secondary Li-ion batteries realized to date, were specifically designed for *in situ* electrical testing in a field-emission scanning electron microscope and/or transmission electron microscope. The results of electrochemical testing were described in detail in previous publication (*Nano Lett.*, 2012, **12**, 505-511). The model Li-ion batteries allow correlation of electrochemical properties with their structural evolution during cycling being analyzed in various imaging, diffraction and spectroscopic modes down to the atomic level. Employing multimode analytical scanning/ transmission electron microscopy imaging coupled with correlative multivariate statistical analysis and tomography, we have analyzed and quantified the 3D morphological and structural arrangement of the batteries, including textured platelet-like $LiCoO_2$ nanocrystallites, buried electrode-electrolyte interfaces and hidden internal defects to clarify effects of scaling on the battery's electrochemical performance. Characterization of the nanoscale interfacial processes using model heterostructure nanowire-based Li-ion batteries provide useful guidelines for engineering of prospective nano-sized building blocks in future electrochemical energy storage systems.

Introduction

Recent developments in nanostructured materials for electro-chemical energy storage (EES) systems have demonstrated the potential to dramatically increase both energy capacity and power density[1-4]. These developments include use of novel electrode materials, such as layered Li transition metal oxides and polyanionic compounds for cathodes and Si, Si/CNT, transition metal oxide nanowires (NWs), Si-carbon composite nanoparticles, fibers, NWs and graphene for anodes as well as Li-S (air) batteries with mesoporous active carbons, etc.[1-4]. EES technologies cover diverse applications ranging from electrical vehicles with large distance range of action (>400 miles), high-altitude long-endurance unmanned aerial or ground vehicles to portable electronics, handheld tools, and implantable medical devices. These emerging applications require long-cycle life high-energy density light-weight rechargeable batteries with the capacity higher by an order of magnitude than those in existing Li-ion/polymer batteries (>1000 mAh/g) and specific energy density over 400 Wh/kg[2,5]. Rechargeable all-solid-state Li-ion batteries (LiBs) with small footprint, on the other hand, are particularly attractive to power an emerging class of autonomous micro- and nano-electromechanical systems (MEMS/NEMS) and related optoelectronic or hybrid devices. Unlike conventional batteries, thin film solid state LiBs can be integrated directly in IC circuit packages alone and/or in the combination with other thermal, motion, vibration and electro-magnetic radiation energy harvesting devices potentially in any shape or size. Additionally, LiBs can be fabricated on flexible plastics by microelectronics integration technology[6]. The latter, however, often suffers from high impedance due to reduced Li conductivity of the solid state electrolyte, as compared to liquid electrolytes[6], and therefore lower discharge efficiency when compared to conventional LiBs. Therefore the utilization of an active material and performance of the batteries at continuous high current discharge should be further improved via better cell design, smaller dimensions and more complex structures for electrode materials[5].

Novel high surface area battery architectures with functional interfaces that are interpenetrating in 3D are currently considered, e.g. trenches, inverse opals, vertical rods, self-similar arrays and a periodic 'sponge'[2,7-9]. It is expected that advanced 3D designs will enhance the battery performance as compared to traditional 2D batteries by amplifying areal energy density while maintaining fast charge transfer kinetics and small footprint. Furthermore, deeper insights into mechanisms associated with charge transfer, nanoscale structural and phase transitions in the battery electrodes are needed to provide new breakthroughs in EES technologies. Among all instrumental methods used for these purposes, scanning and transmission electron microscopy (S/(T)EM) and associated techniques (diffraction, electron energy-loss (EEL) and energy-dispersive X-ray (EDX) spectroscopies, tomography, holography, etc.) play an increasingly important role. Electron microscopy techniques are widely applied for the determination of structure - property relationships in EES materials by obtaining morphological, crystallographic and local chemical information down to the atomic

level[10-20]. S/TEM methods permit real-time examination of various types of batteries during galvanostatic (GS) testing of charge/discharge electrochemical reactions. These methods can additionally probe compression effects and the formation and spatial distribution of the solid-electrolyte-interphase (SEI) under varying processing conditions (temperature, pressure) *in situ* and ex *situ*[4,21-24]. The research can be conducted using environmentally protected loading/transfer cell holders specifically designed for characterization and electrochemical processing of air-sensitive battery materials[21,23,24]. A MEMS-based platform utilizing sealed and open flip-chip assemblies for performing electrochemical measurements with volatile electrolytes inside a TEM has been proposed[25]. NW-based LiBs have been assembled inside TEMs for the purpose of cycling coupled with structural characterization *in situ*[26-30] or for modification, e.g., electrochemical welding in cross-contacted Si NW electrodes during cycling[31]. In reported configurations, however, only NW-based working electrodes (SnO_2, Al or Si) were electron transparent. In these studies, the $LiCoO_2$ or Li counter electrodes were bulk limiting the analyses to anode half-reactions only. Also these one-of-a-kind nanobatteries could not be integrated into a microsystem, nor were their current-voltage-time (*I-V-t*) characteristics reported. Alternatively, thin cross sections of thin film batteries have been imaged in the analytical S/TEM[11,32]. While extremely informative, they are prone to ion beam damage from dual beam focused ion beam (DB-FIB) sample preparation and do not capture the radial geometry characteristic of most 3D LiB designs. To be suited for electrical testing in a TEM *in situ*, the complete thin film nano-battery should have small dimensions (about 10 μm x 30 μm x 100 nm) and therefore the working current should be in the range of a few pA. The latter is necessary to ensure that the actual current density will not exceed a few or tens of mA/cm^2; otherwise the LiB will rapidly fail catastrophically[32].

Single NW-based electrochemical devices have the potential for probing the intrinsic origin for fading of electrode capacity, thus making possible to establish correlations between electrical transport, structure and electrochemical properties in Li-ion-based EES systems[33]. The effects of collective behavior characteristic of large arrays existing in real batteries could be eliminated in individual nanobatteries. This may simplify interpretation of results and reduce the probability that fabrication defects could lead to a catastrophic failure. The small dimensions enable imaging of the entire NW-LiB in a field-emission SEM (FESEM) and/or S/TEM during electrochemical cycling in a pA range[18,19]. Such approach involving mini-NW-LiBs can constitute a powerful engineering platform for diagnostics of nanoscale electrochemical processes that offers highly attractive opportunities for:

(a) cross-instrumentation coordination, and comparison of employed imaging, diffraction and spectroscopy S/TEM and FESEM modes;

(b) selection and optimization of prospective designs and individual components of LiBs, fabrication and assembling of nano-batteries with essential parts transparent to electrons (e.g., Au-catalyzed growth of uniform Si NWs and ordered NW arrays, deposition and processing of thin layers of cathode, anode, electrolyte materials);

(c) DB-FIB-assisted battery integration using MEMS-based inter exchangeable chips compatible both with S/TEMs and FESEMs;

(d) low-current electrical testing *in situ* complemented by modeling of battery's performance under desirable operating conditions.

Here, we report on a 3D S/TEM and tomography characterization of miniature diagnostic all-solid-state LiBs composed of a metal-covered Si NW core utilized as a scaffold for the entire battery and radially deposited $LiCoO_2$ (cathode), lithium phosphorus oxynitride (LiPON, electrolyte) and amorphous Si anode shells. $LiCoO_2$ is a well-known cathode material commonly used in LiBs due to its high capacity, high operating voltage and long cycle-life[2]. LiPON is a solid electrolyte with the highest reported ion conductivity of 2.3 x 10^{-6} S/cm at 25° C[34], it is stable up to 5.5 V *vs*. the Li/Li^+ reference electrode, and does not require a protection layer[35,36]. As anode material for LiBs, silicon received much attention due to its high capacity, corresponding to 4212 mAh/g in $Li_{4.4}Si$, ($4.4Li + Si = Li_{4.4}Si$)[1]. However, the large volume anisotropic expansion of over 300% due to the formation of various Li_xSi_y phases and the ionic character of the bulk Si result in enormous mechanical stress that lead to its rapid pulverization during the first few charge-discharge cycles and loses of electrical integrity. The radial Si NW (core) - $LiCoO_2$/ LiPON/Si multishell heterostructure LiBs were assembled for electrical testing and examination in a FESEM and/or S/TEM. The electrical testing results of these smallest, complete secondary all-solid-state batteries realized to date were described in prior work[37]. We have found that the performance of such NW-LiBs strongly depends on the morphology, structure and phase compositions of the metallized core and cathode and electrolyte shells which have not been previously quantified. In this work, we discuss the role of Si NWs as primary structure scaffold followed by analysis of a NW-LiB's radial core-multishell heterostructure arrangement in relation to its fabrication, and the down-size scaling effects on the battery's electrochemical performance.

Experimental

Synthesis of components and battery fabrication

Si NWs were grown in a hot-walled chemical vapor deposition (CVD) system at 900 °C and 600 Torr using $SiCl_4$ vapor diluted by H_2/N_2 mixture. A vapor-liquid-solid (VLS) growth was catalyzed by 100 nm Au nanoparticles dispersed on *n*-Si (111) substrates functionalized with poly-L-lysine. Gold catalyst nanoparticles were then removed using an aqueous $KI-I_2$ etchant. After removal of the catalyst nanoparticles, the NWs were coated with a 10 nm Ti, followed by 30 nm Pt, 40 nm Ti, and 180 nm-thick layer of $LiCoO_2$. All layers have been deposited using RF and DC sputtering in the same chamber without exposure to air. The coated NWs were annealed in oxygen at 700 °C for 2 hours. Following annealing, the samples were sputter-coated with LiPON of 110 nm to 180 nm in thickness, and finally with about 35 nm of phosphorus-doped *a*-Si anode layer.

For electrical measurements, we contacted individual NW-LiBs dispersed on a Si wafer coated with 600 nm thick thermal oxide. Ion-beam milling was used to expose the Ti/Pt/Ti cathode current collector near the narrow end of the NW-LiB, followed by electron beam induced deposition (EBID) to connect the anode and cathode to lithographically defined metal pads. A 'ring' of the amorphous Si anode was removed near the cathode contact with a DB-FIB to electrically isolate the anode and cathode. In a similar fashion, several NW-LiBs could be dispersed and contacted on silicon chips with 50 nm-thick SiN_x membrane windows and Au contact pads for subsequent examination and/or electrochemical cycling in the S/TEM.

Materials characterization

As-fabricated NW-LiBs were analyzed using a cold field-emission gun Hitachi S4700 FESEM equipped with an Oxford high-speed 80 mm^2 Tmax silicon-drift (SDD) energy-dispersive X-ray detector. Medium and high-resolution S/TEM imaging, selected-area electron diffraction (SAED), and energy-dispersive X-ray (EDXS) analyses

were performed in a Schottky field-emission FEI Titan 80-300 analytical S/TEM with an information limit below 0.1 nm equipped with S-TWIN objective lenses and operating at 300 kV accelerating voltage. For high spatial resolution nanoanalyses in the STEM mode, the instrument was supplied with a Fischione 3000 model HAADF detector, FEI bright-field (BF-) and annular dark-field (ADF-) STEM detectors, a 30 mm^2 EDAX Si/Li EDX detector with a 0.13 srad acceptance angle and a Gatan Enfina electron energy-loss spectrometer. To ensure optimal counting rates, the specimens were tilted 15 degrees towards the EDX detector. To reduce a beam-induced damage of the LiBs (LiPON appeared to be particularly sensitive to electron-beam radiation), the lowest electron beam doses were used as well as beam blanking between acquisitions during imaging and analyses. Tilt-series for STEM tomography were acquired with ±70° tilt angle and step of 2° and then aligned. For reconstruction, a simultaneous iterative reconstruction technique (SIRT) was applied using the FEI Xplore3D/ Inspect3D software suite. Segmentation was performed manually to define the features to produce the tomographic surface rendering of the reconstruction using Amira Visualization Software.

Results and Discussion

Single crystalline silicon NWs as a scaffold and radial heterostructure battery design

High-aspect-ratio semiconductor NWs are considered as primary building blocks for assembling of prospective nanoscale devices and interconnects in future nanoelectronics, nanophotonics and high-performance anode materials for LiBs[1,38,39]. Si NWs are especially attractive because their size (diameter, length) and shape as well as electronic, mechanical, and optical properties can be controlled during synthesis in a predictable manner. Functionality of NW nanoscale devices can be further advanced by creating compositionally modified semiconductor and/or metal/ semi-conductor heterostructures either along the wire as axial hetero-structures, or radially as core-shell NW heterostructures.

Since Si NWs are used here as a scaffold for fabrication of nano-batteries, the ability to grow large arrays of vertically oriented uniform Si NWs is essential to achieve uniform conformal coating of NWs with different electrode layers which constitute a NW-LIB.

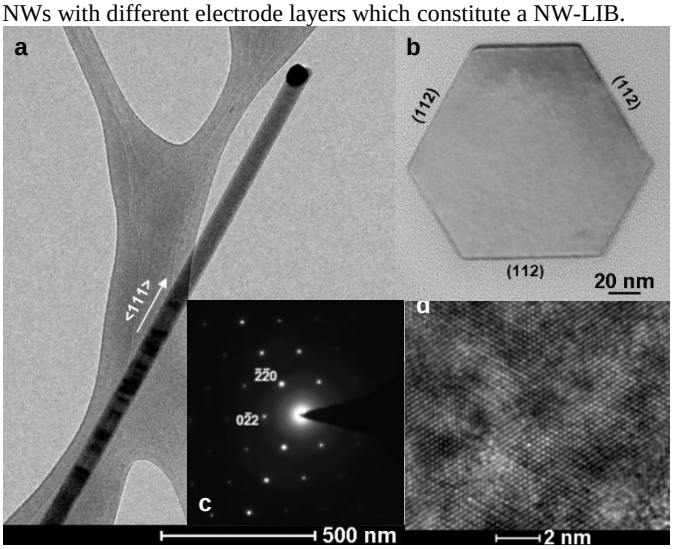

Fig. 1. VLS-grown uniform single-crystalline <111> Si NWs: (a) Bright-field (BF-) TEM, as grown Si NW with a 100 nm Au speck. (b) a {112} faceted cross-section of a Si NW. (c) SAED, a NW's cross-section, {220} point reflections at the [111] zone axis. (d) HRTEM, a Si NW cross-section near its edge displays {220} lattice fringes.

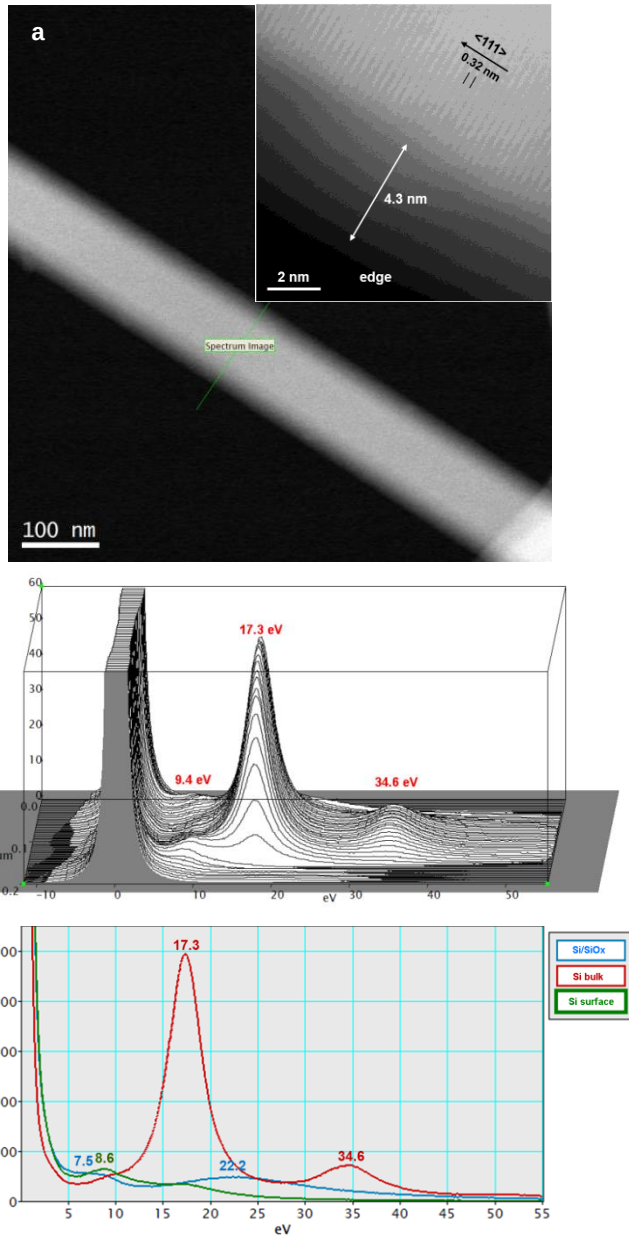

Fig. 2. A single-crystalline <111> Si NW: (a) HAADF-STEM, an enlarged upper inset in (a)) shows zoom of an edge region with 0.32 nm Si (111) lattice fringes near the NW edge, a native oxide layer and no visible defects. (b) 3D STEM-EELS spectral line profiling acquired along green line in (a). (c) Plasmon resonance line shapes for different modes used to assign peaks from (b) indicate surface and bulk Si plasmons at 8.6 eV (green line, c), 17.3 eV and 34.6 eV (red line, c), respectively; Si/SiO_x interface plasmon and 7.5 eV and SiO_x plasmon at 22.2 eV (blue line, c), respectively.

The use of commercially available monodispersed Au nanoparticles resulted in a narrow diameter distribution of NWs (Figs. 1 and S1, Supplementary Information). A secondary electron image in Fig. S1 shows uniform slightly tapered Si NWs arrays grown on a (111) Si wafer. Predominant vertical growth was facilitated by applying a two-stage VLS growth procedure reported earlier[40]. 130 nm to 170 nm diameter <111> Si NWs with 50 to 100 nm Au particles at the tip appear often bent along the axis (Fig. 1a). A typical Si NW cross-section is hexagonal in shape with {112} facets (Fig. 1b). The SAED pattern in the [111] zone axis (Fig. 1c) exhibits {220} point

reflections indicating a defect-free single crystalline structure of the diamond cubic type (Fd-3m space group). HRTEM observations (Fig. 1d) display two-dimensional 0.20 nm to 0.21 nm {220} lattice fringes near the NW edge which appear somewhat expanded as compared to 0.19 nm value for bulk silicon. HAADF STEM image of a Si NW in Fig. 2a shows an inverted contrast as compared to the BF-TEM image in Fig. 1a. High-resolution HAADF-STEM (inset) displays a side view of a NW with 0.32 nm (111) silicon lattice spacing with no visible defects and 3 nm to 4 nm-thick native oxide shell. The native oxide shell was confirmed by EDXS and EELS analyses (see Fig. S2, Supplementary Information and Fig. 2c, respectively).

A 3D plot of EEL spectra (Fig. 2b) was obtained from a line scan across an isolated, suspended single-crystalline Si NW of 120 nm in diameter over a large range of thicknesses ranging from 0 to about 0.8 of an inelastic mean free path for the 300 kV incident beam. The spectra at the ends near 0 and 190 nm are aloof in vacuum, those at 25 nm and at 130 nm are just grazing the surface, and those in between are penetrating the NW's bulk. The bulk EEL spectra consist of bulk plasmon peaks at integer multiples of 17.3 eV (the first plasmon) and of 34.6 eV that correspond to the second plasmon. Interestingly, the Im $(-1/\varepsilon)$ bulk energy-loss function predicts no peaks below 17.3 eV in silicon[41]. However, as the beam reaches and passes the edge of the material, the bulk plasmon peaks disappear very rapidly and are replaced with surface plasmons between 8 eV to 10 eV energy losses (Fig. 2c). According to calculations by Reed et al.[42], the surface plasmon losses include a mixture of azimuthal mode numbers *m* and a direct interband transition at about 5 eV, which cannot be clearly separated from the background for such large NW diameter. The peak 7.5 eV is assigned to a Si/SiO_x interface plasmon, which in the aloof mode

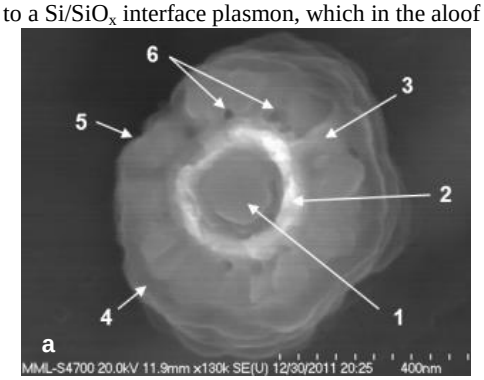

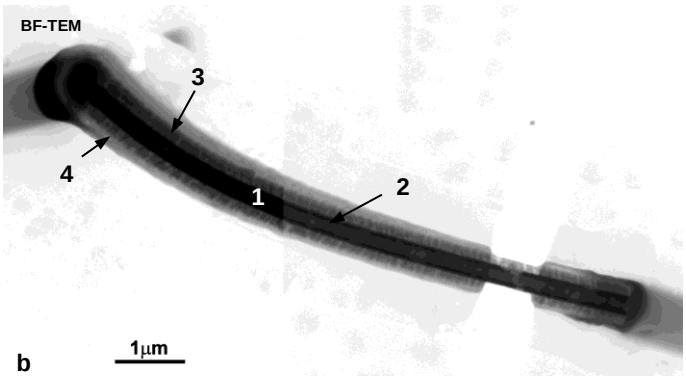

Fig. 3. (a) FESEM, a NW-LiB's cross-section. (b) BF-TEM montage, a NW-LiB contacted with Pt pads, a cut was made by DB-FIB to reduce a leakage through the supporting silicon nitride membrane. 1 - (111) Si NW, 2 - Ti/Pt/Ti metal collector layer, 3 – platelet-like $LiCoO_2$ crystallites in a cathode layer, 4 - LiPON electrolyte layer, 5 - *n*-Si amorphous anode layer, 6 - voids.

also may be due in part to retardation effects[43]. The wide peak at about 22.2 eV corresponds to a bulk plasmon in SiO_x itself[44]. In summary, S/TEM imaging combined with high-spatial resolution EDXS/EELS analyses indicate possibilities for atomic-scale monitoring of NW structures, i.e. shapes, crystallinity, native or thermally induced insulating surface oxide layers, compositions, and electronic properties, which are critical for producing defect-free uniform functionalized NWs with controlled mechanical and transport properties.

In order to understand how LiBs behave at reduced dimensions, we have created complete nanobatteries using Si NWs as a primary scaffolding structure onto which the various battery components are deposited sequentially by sputtering. $LiCoO_2$ (cathode), silicon (anode) and LiPON (solid electrolyte) have been selected based on (a) their well-known electrochemical performance in macroscopic all-solid-state Li-ion EES systems[35,36] and (b) to realize the advantages of a radial NW core-multishell heterostructure geometry regarding mitigation of the mechanical stress caused by significant volume expansion in silicon anode. Secondary electron images collected at different stages of fabrication are shown in Figs. S3a-c, Supplementary Information, respectively. Each NW-LiB consists of a Ti/Pt/Ti metalized core current collector coated with $LiCoO_2$ (cathode) and annealed at 700 ^oC, followed by deposition of a LiPON solid electrolyte, and an *n*-doped amorphous Si anode (Figs. 3a and b). Structural analyses performed after fabrication confirmed that following annealing $LiCoO_2$ was crystallized in the hexagonal phase (R-3m space group)[37]. The proposed battery fabrication scheme enables simultaneous production more than 10^6 cm^{-2} nearly identical batteries (Fig. S3d, Supplementary Information). Figs. S3e and S3f, Supplementary Information present cumulative and differential histograms on NW-LiB's maximum diameter (d_{max}) and length (l) distributions, respectively. For count number, N = 300, the histograms point to the high uniformity of the LiBs with parameters close to those for the normal distribution with the average aspect ratio of 5.5. A montage of BF-TEM images (Fig. 3b) shows the assembled integrated NW-LiB on a SiN_x membrane. At 0.5 μm to 1.2 μm in diameter and up to 7 μm in length, these all-solid-state NW-LiBs are the smallest, complete secondary batteries realized to date.[37]

Multimode analytical STEM imaging and electron tomography of individual NW-LiBs

This is a real challenge to visualize an internal structure of an individual NW-LiB due its complex core-multishell radial heterostructure arrangement, multiphase composition and large thickness. Using a series of detectors operating in selected ranges of collection angles, it is, however, possible to acquire multiple STEM signals for the same (pixel) position, which are compatible with the enhanced micro- and nano-analysis capabilities. A montage of STEM images of a NW battery (Fig. 4) recorded simultaneously in BF-, ADF- and HAADF-STEM modes shows its internal microstructure and demonstrates the value of multimode STEM imaging with the combination of detectors covering a wide range of scattering angles. Various contrast mechanisms and strong contrast variations resulting in complete contrast reversal (e.g., compare BF- and ADF-STEM images in Fig. 4a) reveal clearly important nanoscale features, i.e., textured platelet-like $LiCoO_2$ nano-crystallites, 80 nm to 120 nm-thick pinhole-free LiPON layer, and buried electrode-electrolyte interfaces even in 0.5 to 1.5 μm–thick areas. The STEM offers evident benefits over the broad-beam illumination TEM, which normally requires thin samples less than 100 nm in thickness (e.g., see Fig.3c and Fig. 4b). The main advantage for nano-batteries is that the HAADF signal is generated

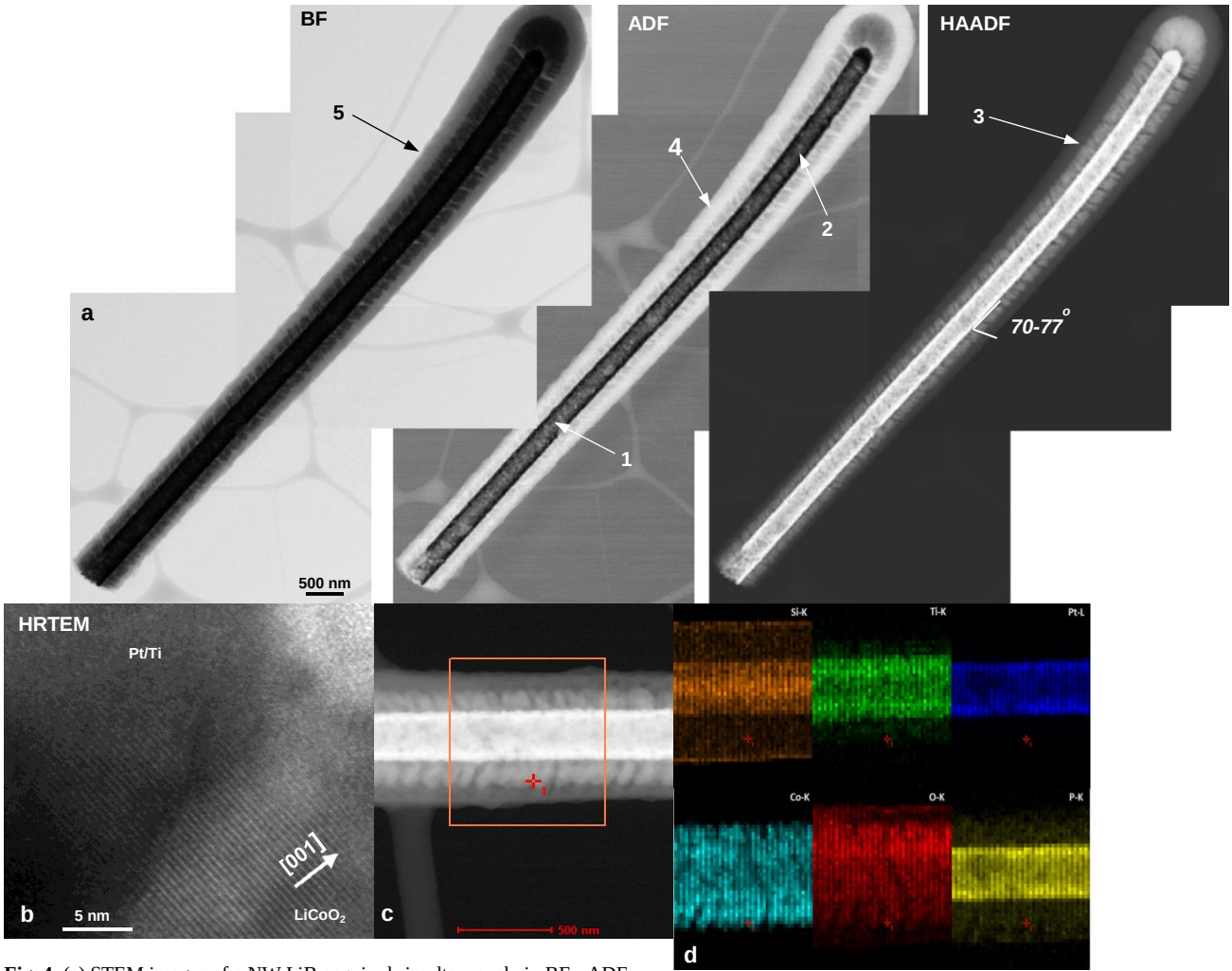

Fig. 4. (a) STEM images of a NW LiB acquired simultaneously in BF-, ADF- and HAADF modes, respectively. Multimode STEM reveals an internal microstructure in 0.5 nm to 1.5 μm–thick NW-LiBs, including 160 to 200 nm-long $LiCoO_2$ crystallites tilted by 70 ° to 77° against the metallized NW surface, 80 nm to 120 nm pinhole-free LiPON layer and buried $LiCoO_2$-LiPON and LiPON-Si electrode-electrolyte interfaces. 1 - (111) Si NW, 2 - Ti/Pt/Ti metal collector layer, 3 - $LiCoO_2$ cathode layer, 4 - LiPON electrolyte layer, 5 - *n*-Si amorphous anode layer. (b) HRTEM, a NW-LiB's cross-section, a rough metal collector - $LiCoO_2$ interface demonstrating 73° tilt orientation of (003) planes with 0.48 nm spacing in a hexagonal layered $LiCoO_2$ nanocrystallite with respect to the metal film. (c) HAADF-STEM, a NW-LiB fragment. (d) Drift-corrected EDXS SI data acquired over the fragment marked by orange box in c.

by the incoherent Rutherford-like electrons scattered out to high angles, in which the registered images have different levels of contrast related to the atomic number (chemical composition), the density and thickness (mass-thickness) of the battery component[45]. In STEM, partial temporal coherence may arise only because of the relatively low spread in energies of the illuminating beam if field emission sources used[46]. Contrary to TEM, STEM imaging is not limited by the spherical aberrations of the objective lens, which may cause contrast delocalization[47]. In addition, STEM enables higher contrast and less blurring in thick specimens at least up to 1.5 μm in particular case. With sufficiently small convergence angles of the incident beam (1 to 2 mrad), one can increase depth of field so that the entire thick sample will be in focus along its depth, i.e., z-direction. Utilizing an axial BF-detector instead of a HAADF-detector reduces blurring of specimen features situated toward the bottom of thick samples. Even if diffraction effects are not completely avoidable, Z-contrast in the incoherent HAADF-STEM mode relates the image intensity monotonically to the atomic number, material density and thickness making a much better approximation to a mass thickness image than a coherent BF image[45]. The ability of HAADF-STEM to suppress diffraction and phase contrast, however, makes it insensitive to differentiating between crystalline and amorphous phases. Conversely, phase contrast BF-STEM provides both crystallographic and orientation relationship information. Ideally, by recording multiple STEM signals and analyzing correlations between the image intensity and elemental compositions, one can identify and ultimately quantify LiB's phase composition. Drift-corrected EDS X-ray maps (Fig. 4d) acquired on the NW-LiB fragment marked by orange box in HAADF-STEM image (Fig. 4c) confirm elemental compositions of the major components, including metallized core (Si-K, Ti-K and Pt-L X-ray maps), $LiCoO_2$ cathode (Co-K and O-K X-ray maps), LiPON solid electrolyte (O-K and P-K X-ray maps) and thin outer-shell *n*-Si layer (Si-K X-ray map) as well. Note that the intensity of the P-K line at 2.02 kV in the core region is artificially enhanced by overlapping with the Pt-M series (the Pt $M\alpha_1$ at 2.05 keV) and therefore the resulting phosphorus map does not reflect its actual elemental composition.

Correlative multivariate statistical analysis (MSA) used to analyze large datasets of multimode STEM images provides effective means for systematic multiparameter data evaluation and an unbiased classification of the phases[48-50]. In MSA, one can define

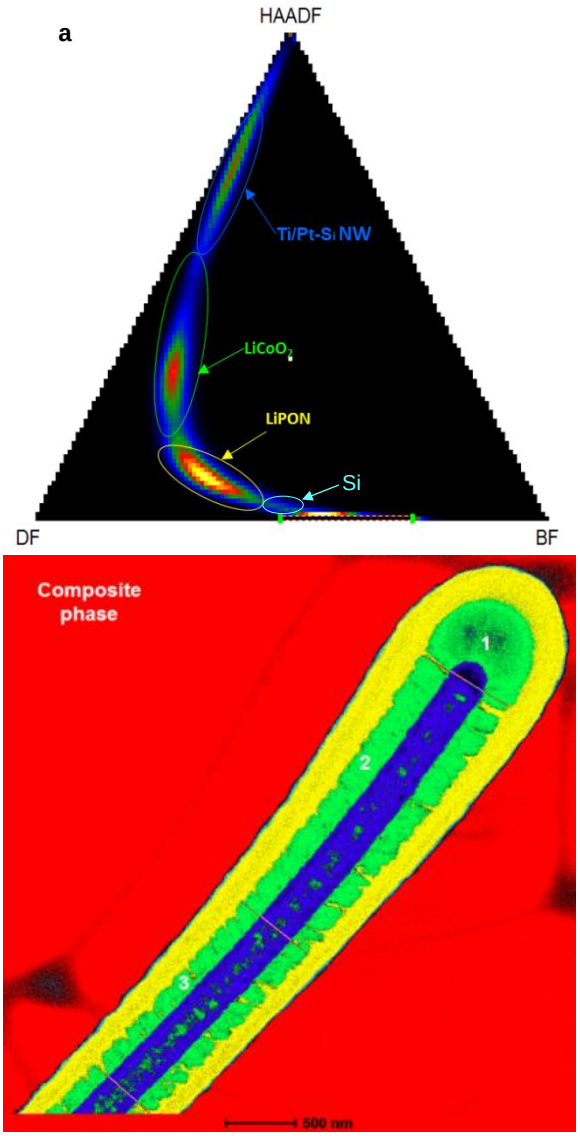

Fig. 5. Correlative MSA of BF-, ADF- and HAADF-STEM images of the NW-LiB shown in Fig. 4a. (a) Trivariate histogram of STEM intensities distribution with a resolution r = 128 pixels reveals distinct clusters of the major phases with the subtracted background (red). (b) Composite image showing extracted phases in line with EDXS SI data in Fig. 4d: metallized Si NW (blue), $LiCoO_2$ cathode (green), LiPON electrolyte (yellow) and Si anode (light blue). Red lines mark parts 1, 2 and 3 (see Table 1 for details.

an image by its components along the axis chosen in a hyper-dimensional space with as many dimensions as there are pixels in the image. It seeks correlations between the number of components and the "fingerprint" image or concentration of each component. Such components should be incorporated in a set of imaging and/or spectral data recorded from the samples in which the compositions of the constituent phases may vary with spatial positions[13,51]. In the present study, we have adopted multivariate scatter diagram construction using earlier described analysis routines[50] in order to quantify spatial correlations between the intensities of three different input STEM signals and NW-LiB's phase compositions. When considering the correlations between two or more images, the points could be distributed over an ideal curve corresponding to the ultimate correlation; the distribution width reflects the contribution of the statistical noise. A trivariate scatter histogram of STEM

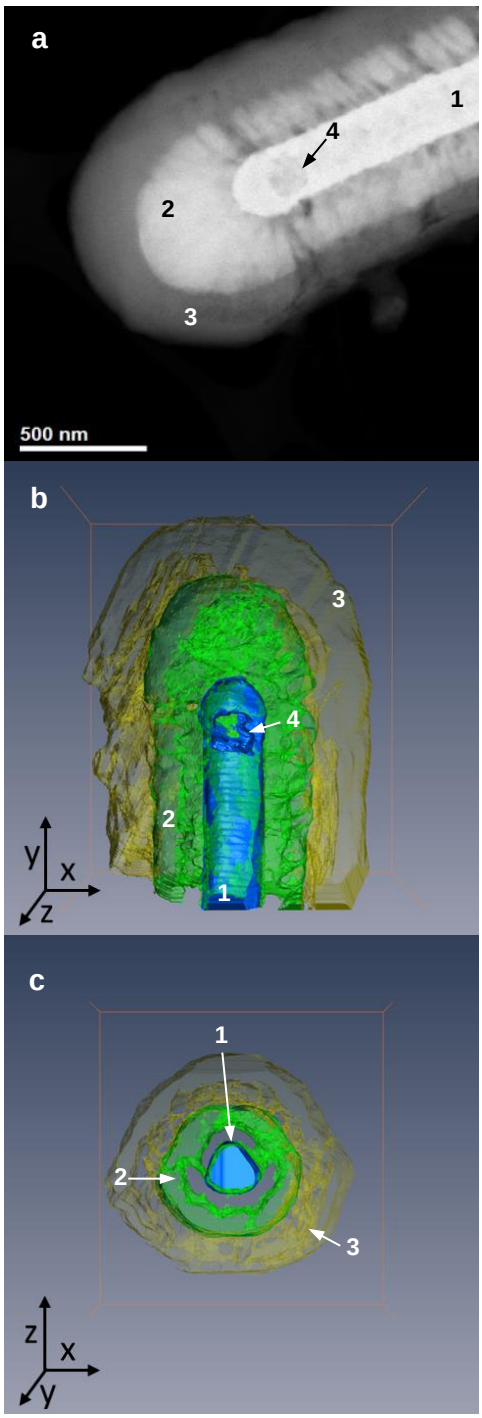

Fig. 6. High-tilt STEM tomography of a pristine NW-LiB: (a) HAADF-STEM, a single frame extracted from a tilt-series. (b) The reconstructed and segmented 3D side view of a NW-LiB's tip showing lateral distribution of $LiCoO_2$ crystallites around the metallized silicon NW core. 3D reconstruction of the metallized core reveals a void (4, barely visible in image (a), also shown in enlarged right bottom inset) near the NW's tip likely formed in the process of thermal annealing at 700 ^oC in oxygen due to the reaction with a Pt-Ti metal collector. (c) top view of a 3D overlay of the reconstructed and segmented $LiCoO_2$ shell and the NW core visualizing the complex morphology of a $LiCoO_2$ – LiPON interface (shown in green), where major electrochemical processes occur during cycling. 1 - Si NW with a metal collector layer, 2 - $LiCoO_2$ cathode layer, 3 - LiPON layer covered with an amorphous *n*-Si anode layer. The volume of the bounding box of the reconstruction is (1451 nm by 1500 nm by 1730 nm.

Table 1. Volumes of $LiCoO_2$ and maximum theoretical discharge capacity of an individual NW-LiB (I) and its parts

Part	External diameter, nm	Estimated volume, v x10^6, nm^3	Maximum theoretical discharge capacity, pAh
1 (top head)	610	23.81	0.016
2 (middle)	480	84.17	0.058
3 (bottom end)	423	39.05	0.027
Total	-	147.03	0.10

intensities distribution in Fig. 5a revealed distinct clusters of the major phases with the subtracted background in red. The histogram is generated by comparison of the intensities contained within the source images and a sampling width ***w*** determined by the histogram resolution ***r*** as

$$\boldsymbol{w}_{\text{signal}} = [\max_{survey}(I)-\min_{survey}(I)]/\boldsymbol{r}, \quad (1)$$

where I is the intensities of BF, ADF or HAADF signals, respectively. The intensities are plotted as a fraction of the total sum of intensities for each pixel from the three source images after applying the intensity range limits to the source images and rescaling with the minimum intensity set at zero and the maximum at the specified histogram resolution. Such rescaling allows the contribution of each source image to be independent of its relative intensity. The composite image in Fig. 5b shows the phases extracted in agreement with EDXS SI data in Fig. 4d. Here, the metallized Si NW is in blue, $LiCoO_2$ cathode is in green, LiPON electrolyte is in yellow and Si anode is in light blue. For the NW-LiB's components, MSA indicates the complete structural and compositional correlation that enables phase classification and quantification.

In EES systems the discharge capacity is one of the major parameter of their performance. The maximum expected discharge capacity of the battery can be determined by measuring available $LiCoO_2$ volume. In line with XRD and EBSD analyses[37], $LiCoO_2$ annealed at 700 ^oC in oxygen, corresponds to the electrochemically active α-$NaFeO_2$ type rhombohedral phase (space group R-3m; PDF#75-0532) with lattice parameters a = 0.282 nm and c = 1.405 nm in the hexagonal setting and density ρ = 5.056 g cm^{-3}. Table 1 summarizes results of measurements of volume of three major parts of the NW-LiB as indicated by red lines in Fig. 4b. The maximum expected discharge capacity has been derived from estimated values of volume of $LiCoO_2$ phase according to the following equation:

$$Q = 0.5\ FzV\rho/M, \quad (2)$$

Here, Faraday constant F = 96485.3 C mol^{-1}, number of electrons participating in the charge transfer z = 1, molar weight M = 97.87 g, and V is the estimated volume. It was assumed that only about half of available Li^+ ions could be involved in an intercalation process during cycling without collapsing its crystalline structure. For comparison, the experimental capacity of similar NW-LiB measured with an electrical nanoprobe manipulated inside a FESEM was 0.03 pAh, or 30% of the expected theoretical capacity. The lower measured value can be attributed to the excessive polarization losses due to the rapid discharge and possibly to the presence of passivated $LiCoO_2$ phases which did not contribute to the battery capacity.

In the hexagonal $LiCoO_2$ structure refined by powder neutron diffraction profile analysis, fully ordered Li and Co ions occupy octahedral sites in alternating {111} layers within a face-centered cubic oxygen sublattice. The platelet-like $LiCoO_2$ crystallites of 160 nm to 200 nm in length and 30 nm to 60 nm in width appear to be

Table 2. Volumes of $LiCoO_2$, $LiCO_2$/LiPON phase ratios and maximum theoretical discharge capacity of a NW-LiB (II) and its parts evaluated using electron tomography

Part	External diameter, nm	Estimated volume of $LiCoO_2$, v x10^6, nm^3	Maximum theoretical discharge capacity, pAh	Estimated volume of LiPON, v x10^6, nm^3	$LiCoO_2$/ LiPON volume ratio
1 (top head)	1103	115.73	0.08	344.65	0.336
2 (middle)	1051	131.98	0.09	284.42	0.464
Total	-	247.71	0.17	629.07	0.394

tilted by 70^o to 77^o against the metallized silicon NW surface, thus indicating a texture in the cobaltite layer growing around the metalized NW (Figs. 4a-c). A strong dependency of the $LiCoO_2$ crystal orientation in thin films on the chemical structure of the substrate surface and preferred (003) and (101) orientations for the annealed $LiCoO_2$ films sputtered on bare and oxidized silicon wafers have been reported[35,52]. Due to a layered arrangement of the α-$NaFeO_2$ type rhombohedral structure with Li-O-Co-… layers stacked in the ABC sequence, strong orientation effects significantly influence its electrochemical performance[35]. Because only 2D diffusion paths are available in the layered structure, Li^+ transport through the active electrode can be seriously hindered if a $LiCoO_2$ film is deposited in a strongly preferred (003) orientation. Differences in orientation could result in a variation in Li^+ conductivity of a few orders of magnitude[53]. $LiCoO_2$ nanocrystallites tend to grow in radial directions around the metallized NW core as flower-like flakes occasionally leaving 20 nm to 50 nm voids at the bottom near the interface with the current collector (see Figs. 2d, e and 4a-c). Similar voids were found along a NW-LiB (Fig. 6a). The voids are likely formed under crystallization of $LiCoO_2$ during annealing at 700^o C in oxygen. Noteworthy, $LiCoO_2$ nanocrystallites were uniformly coated with amorphous-like LiPON electrolyte. According to Kim et al.[54], this enables higher capacity retention of up to 90% of the original capacity due to reduction in side reactions that could increase the cell resistance during the cycling.

In addition to traditional 2D S/TEM techniques, single-axis tilt STEM tomography was employed for obtaining detailed quantitative information about the 3D NW-LiB's structural arrangement and its expected discharge capacity. The reconstructed and segmented 3D visualization data (Fig. 6) demonstrate the spatial distribution of $LiCoO_2$ crystallites around the metallized NW core embedded within LiPON. The dimensions of the bounding box are 1500 nm (x) by 1730 nm (y) by 1451 nm (z). Interestingly, the 3D visualization shows the preservation of faceted metallized core (Fig. 6c) and reveals a void near the tip that is defect likely formed during thermal annealing process (a Kirkendall effect, Fig. 6a). This void can also be observed in within specific frames of the high tilt series STEM tomography (Fig. 6a). Due to the geometry of the void, the void is either obscured or less pronounced in specific orientations. The orthogonal alignment then enables a simple numerical integration of segmented reconstructed sections of the desired phase, e.g., along its long axis. Table 2 summarizes measurements of $LiCoO_2$ volume, $LiCoO_2$/LiPON phase ratios and maximum expected discharge capacity of another NW-LiB. The NW-LiB (II) was intentionally modified to increase its capacity as compared to the NW-LiB (I). The data presented in Table 2 indicate that electron tomography enables visualizing and quantification of the complex morphology of

electrode and electrolyte phases in individual NW-LiBs and the maximum expected discharge NW-LiB's capacity is estimated as 0.1-0.17 pAh depending on the available $LiCoO_2$ volume.

Structural model of a radial core-multishell heterostructure NW-LiB and down-size scaling effects on its performance

In a model proposed to describe the radial heterostructure NW-LiB (Fig. 7), platelet-like $LiCoO_2$ nanocrystallites with preferential (101) growth planes are aligned with the Si NW sidewalls, while (003) planes are tilted away from the normal to the NW axis by 10^o to 20^o

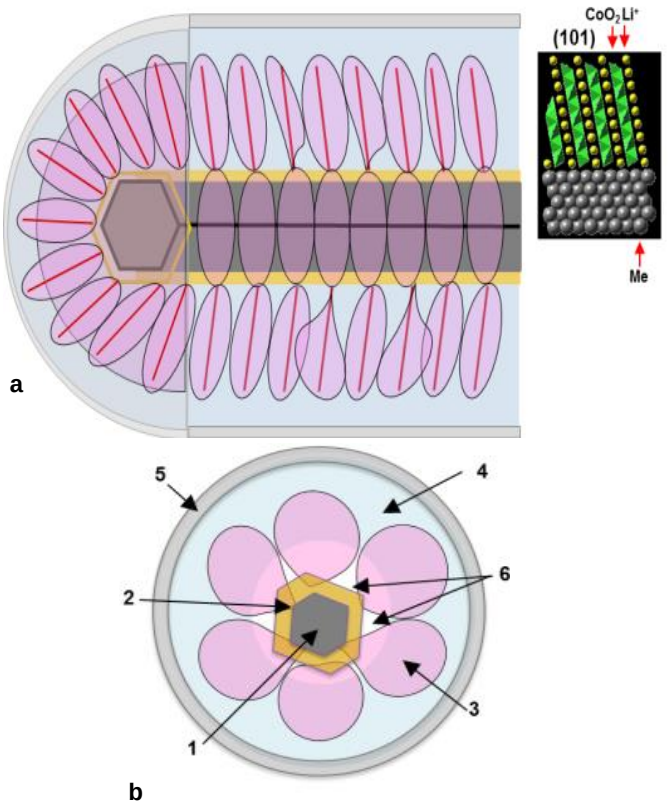

Fig. 7. Schematic of a NW-LIB showing its 3D morphological and structural arrangement: (a) Y-section, an enlarged view of a $LiCoO_2$- metal collector interface (inset). (b) X-section. Red lines parallel to (003) planes indicate directions of preferential growth of $LiCoO_2$ platelet-like nanocrystallites. 1 - (111) Si NW, 2 - metal collector layer, 3 - $LiCoO_2$ cathode layer, 4 - LiPON electrolyte layer, 5 - *n*-Si amorphous anode layer, 6 - voids.

(Fig. 4b). EBSD analysis of the crystallites confirmed that they have rhombohedral R-3m structure and the misorientation angle between $LiCoO_2$ [003] and Si [111] directions was about 8° [37]. HRTEM observations (Fig. 4b), in line with Bohne et al.[52], suggest that there is a tendency that oxidic substrates likely tend to favor a (101) $LiCoO_2$ texture. This is because the preferred film orientation with angle to the substrate[55]. Since Li ion-containing layers are tilted by 70^o to 77^o towards the metallized NW core, such configurations the (*h0l*) plane should possess $LiCoO_2$ grains positioned at some favor the Li^+ ionic transport from the cathode directly to the current collector. Otherwise, for the preferred (003) texture, when most of the grains are oriented with their (003) plane parallel to the substrate and cobalt oxide layers block the direct Li^+ transport to the current collector[35,56]. The latter is consistent with the morphology of hydrothermally grown precisely size-controlled $LiCoO_2$ nano-platelets in the stacking direction of the CoO_2 layers relatively to the basal plane as confirmed by XRD and TEM[57]. For NW-LiBs, the observed texture of submicron $LiCoO_2$ layers is likely governed by the metal substrate/layers interactions. As the metallized Si NW core may be partially oxidized during the deposition and annealing in oxygen, the sputter deposition conditions may essentially influence the surface texture of a $LiCoO_2$ layer.

In situ electrical testing of the NW-LiBs was conducted in a wide range of currents from 0 V to 4.2 V in a FESEM and TEM (see Figs. S4 and S5, Supplementary Information and ref.[37]). Since the FESEM microstructural characterization is limited primarily to the NW-LiB's surface topography, it was complemented by *ex situ* S/TEM examinations. For testing in the S/TEM, MEMS E-chips with a 50 nm SiN_x membrane window and patterned Au electrodes have been used to mount electrically contacted NW-LiBs. Initial *in situ* TEM observations of NW-LiBs biased to 4.2 V (Fig. 4 in ref.[37]) indicated formation of voids at the $LiCoO_2$/LiPON interface, which expanded substantially following eight charge-discharge cycles. The cathode and anode half-reactions during cycling of the solid state $LiCoO_2$/LiPON/Si cell can be expressed as follows[58]:

$$\text{Cathode: } LiCo^{iii}O_2 = Li_{1-x}Co^{iv}O_2 + xLi^+ + xe^- \ (x \le 0.5) \qquad (3)$$

$$\text{Anode: } Si + x'Li^+ + x'e^- = Li_{x'}Si \ (0 < x' \le 4.4) \qquad (4)$$

It is established that Li_xCoO_2 can be reversibly cycled between $0.5 < x < 1$, bringing the gravimetric charge capacity of a $LiCoO_2$ electrode at a theoretical maximum of 137 $mAhg^{-1}$ [9,55]. This is equivalent to a volumetric storage capacity of approximately 700 mAh cm^{-3} for a 0.097 nm^3 $Li_3Co_3O_6$ unit cell[59]. According to Reimers and Dahn[59], for a favorable orientation of $LiCoO_2$ cathode layer with respect to the electrolyte, a flat lithium intercalation/

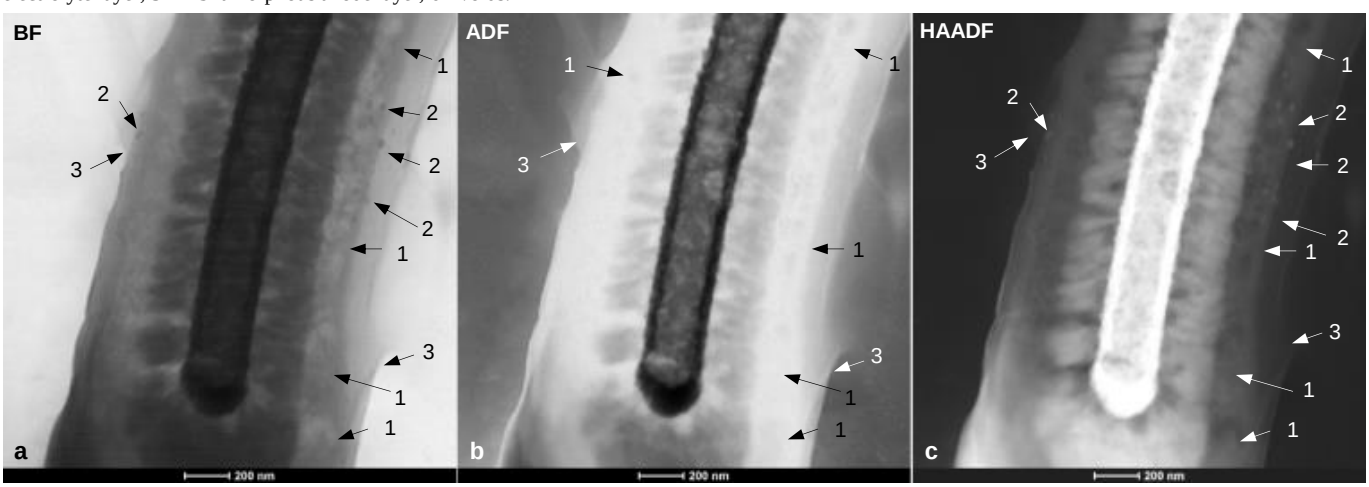

Fig. 8. *Ex situ* STEM, a cycled NW-LiB after 8th discharge. (a) BF-STEM. (b) ADF-STEM. (c) HAADF-STEM. 50 to 100 nm voids (1) at and near the LiPON-$Li_{1-x}CoO_2$ interface, 10 to 40 nm spherical particles (2) located in the LiPON layer and partially delaminated 10 to 50 nm thick *n*-Si anode layer (3) are evident.

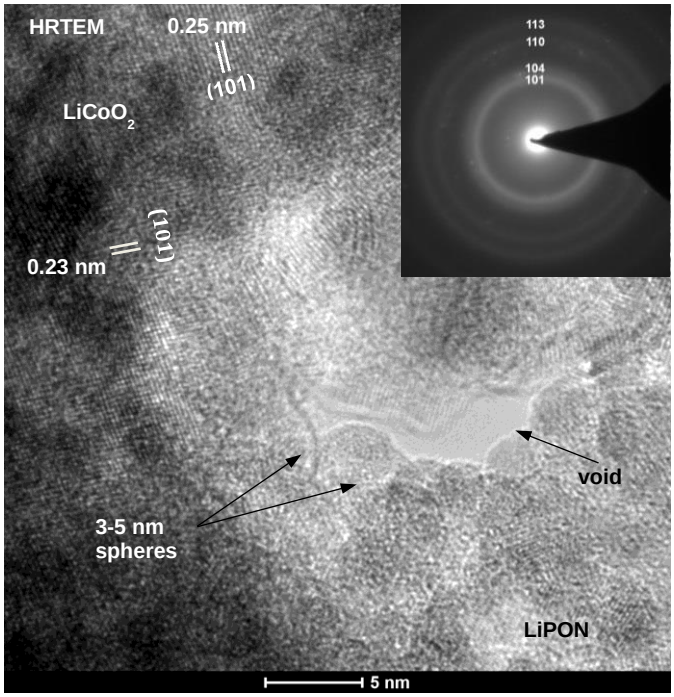

Fig. 9. HRTEM, a thin NW-LiB thin section. an area around a void reveals 5 nm to 10 nm $Li_{1-x}CoO_2$ crystallites with 0.25 nm (101) lattice fringes and 3 nm to 5 nm diameter amorphous particles. SAED pattern (right inset) displaying broadened (101), (104), (110) and (113) ring reflections.

extraction plateau exist around 3.9 V *vs*. a Li/Li^+ reference electrode. The plateau corresponds to a Li content of $0.75 < x < 0.93$ in Li_xCoO_2 and results from the coexistence of two different disordered hexagonal phases[59,60]. In addition, a monoclinic structure of Li_xCoO_2 may appear at higher potentials between 4.1 and 4.2 V. Detailed *ex situ* multimode STEM examination of the cycled NW-LiB (Fig. 8) revealed 50 nm to 100 nm voids (shown by black and white arrows) generated at and near the LiPON- $Li_{1-x}CoO_2$ interface under cycling. Another pristine NW-LIB was also imaged for comparison and it did not show presence of voids. We did not observe further formation of the voids in both cycled and pristine NW-LiBs after several hours of continuous examination using lowest beam intensities to minimize radiation damage. 10 nm to 40 nm spherical particles formed in the LiPON layer during its decomposition and partially delaminated areas of a 10 nm to 50 nm thick *n*-Si anode layer were also found. A drift- corrected X-ray line profile across the cycled NW-LiB (Fig. S6, Supplementary Information) showed reduced intensities of the phosphorus P-K and oxygen O-K X-ray lines at LiPON- $Li_{1-x}CoO_2$ interfaces on the sides of the NW- LiB. Both STEM imaging and EDXS analyses have pointed to breakdown and decomposition of about a 110 nm-thick LiPON layer during initial stages of electrochemical cycling.

Smaller electrode feature dimensions and inter-electrode separation are advantageous for improving power performance by minimizing electron and ion diffusion times and limiting Ohmic losses. Increasing the interface area is beneficial for lowering the local current density and the associated charge transfer overpotentials. The increased interface area requires more electrolyte, which may also function as the electrode separator. Reducing the electrolyte thickness below 1 μm is essential for achieving higher power and energy density 3D LiBs[54]. The deposition of a uniform, pinhole-free electrolyte layer over a potentially complex and high aspect ratio structure may be quite challenging. At thickness much less 1 μm, the ability of the electrolyte to prevent electronic current flow between the anode and cathode and its chemical stability, however, may be drastically compromised due to onset of space charge limited conduction (SCLC)[61]. The origin of the electronic current was clarified via detailed examination of the NW-LIB's I-V characteristics by slow scan linear voltammetry (see Figs. S4 and S5, Supplementary Information). In the SCLC regime, there is a steep dependence of the leakage current on thickness as $j \propto d^{-3}$. For thicker electrolyte layers, larger threshold voltage V_1^* was found although the increased values were less than predicted by a d^2 dependence likely due to the combination of the non-uniformity in the LiPON layer thickness and the roughness in the $LiCoO_2$ SCLC is a bulk limited transport mechanism, implying facile injection of charge at the LiB's contacts ($LiCoO_2$ and Si in the present case). Finally, it was found excellent agreement between experimental and calculated I−V characteristics for the NW-LIB with thickness of the LiPON electrolyte layer of 110 nm. A large electronic current has been reported for a 1.5 □m thick LiPON layer sandwiched between Pt electrodes (a Li-ion blocking metal) at a potential of about 5.5 V, concomitant with formation of bubbles at the positive electrode[34]. A pronounced change in the impedance characteristics suggests the formation of an interfacial layer with large capacitance. The bubble formation and apparent breakdown of LiPON were assigned to the chemical reaction involving the cleavage of P-O bonds, formation of P-O-P chains, and generation of oxygen[34]:

$$2Li_3PO_4 = Li_4P_2O_7 + 1/2O_2 + 2e^- \quad (5)$$

Ex situ TEM examinations of the NW-LiB's thin section (Fig. 9) have provided further details on nanoscale transformations occurring during the breakdown of LiPON. The SAED pattern (Fig. 9, right inset) displays diffuse (101), (104), (110) and (113) ring reflections but practically no most intensive (003) reflections. This is because $Li_{1-x}CoO_2$ crystallites were disrupted due to cation disordering under cycling followed with the formation of disordered hexagonal phases[60]. Around a void, we have observed $Li_{1-x}CoO_2$ crystallites with 0.23 nm to 0.25 nm (101) lattice fringes and 3 nm to 5 nm diameter amorphous-like particles formed during the electrolyte breakdown.

Conclusions

Semiconductor NWs are highly attractive as building blocks in novel 3D multifunctional EES architectures that maximize areal energy density. Single-crystalline NWs can be grown directly on the metallic current collector providing improvements in rate capabilities in metal oxide cathodes due to efficient 1D electron transport, reduced defects, and facile strain relaxation. In this work, we have characterized radial core-multishell heterostructure NW-LiBs designed for low-current electrical testing in FESEM and/or S/TEM. Such diagnostic batteries allow correlating electrical transport properties tailored for specific electrochemical performance with the structure on the same NW. At 0.5 μm to 1.2 μm in diameter and up to 7 μm in length, these all-solid-state NW-LiBs are the smallest, complete secondary batteries realized to date. The individual pristine and cycled NW-LiBs have been analyzed using the combination of imaging, diffraction and spectroscopic S/TEM modes down to the atomic level. Multimode analytical STEM imaging coupled with correlative MSA and high-tilt angle STEM tomography have been used to clarify the 3D morphology, chemical distributions (phases), and structural arrangement of the NW-LiBs. This can further expand capabilities for meso- and nanoscale phase and interface analyses of inhomogeneous nanostructural composites, which could be difficult or impossible to analyze using conventional TEM, electron diffraction or EELS

because of the large thickness, complex morphologies and overlapping phases. Due to reduced image blurring and significant contrast variations which were obtained even in 1.0 μm to 1.5 μm thick LiBs, we have visualized and quantitatively analyzed the phase compositions and internal microstructures of deposited electrode layers, including platelet-like $LiCoO_2$ crystallites and buried electrode-electrolyte interfaces. The texture of thermally grown hexagonal $LiCoO_2$ nanocrystals of 160 nm to 200 nm in length and by 30 nm to 60 nm in width with preferential orientations of Li-containing layers towards the core is favorable for direct Li ion transport from and into the cathode interior and to the current collector with respect to the direction of current flow in a NW-LiB. Using high-tilt angle STEM tomography, we have revealed hidden defects such as a void near the NW tip likely formed during annealing due to the reaction with the Pt-Ti metal collector (a Kirkendall effect) and visualized the complex morphology of a $LiCoO_2$ – LiPON interface, where major electrochemical processes occur during cycling. Illustrating the importance of the metal substrate/electrode and electrolyte layers interactions, these findings provide useful guidelines for engineering of large interfacial area electrode/ electrolyte interfaces. Controlling textures of nano-crystalline $LiCoO_2$ layers, one can potentially promote efficient Li-ion transport within sufficiently short diffusion length and create large interface area 3D electrode-electrolyte architectures with low-resistance. We intend to apply this platform for *in situ* diagnostics of nano-sized building blocks of composite electrodes and other key components in future 3D EES designs that could be suitable both for a large scale-up synthesis and fabrication using existing semiconductor technologies.

Acknowledgements

Authors are thankful to J. Winterstein and A. Herzing (NIST) for help in measurements and useful discussions and to A. Kolmakov (NIST) for critical reading of the manuscript. This work was supported by the National Institute of Standards and Technology under Grant MML12-1053-N00 (Award No 70NANB12H164). D.R. acknowledges support under the Cooperative Research Agreement between the University of Maryland and the National Institute of Standards and Technology Center for Nanoscale Science and Technology, award 70NANB10H193, through the University of Maryland. AAT and JC were supported (and VO was partially supported) by the Science of Precision Multifunctional Nanostructures for Electrical Energy Storage (NEES), an Energy Frontier Research Center funded by the U.S. DOE, Office of Science, Office of Basic Energy Sciences under award DESC0001160. Sandia is a multi-program laboratory operated by Sandia Corporation, a Lockheed Martin Company, for the U.S. DOE National Nuclear Security Administration under Contract DE-AC04-94AL85000.

Notes and references

[a]Material Measurement Laboratory and [b]Center for Nanoscale Science and Technology, National Institute of Standards and Technology, Gaithersburg, Maryland 20899, United States
[c]Institute for Research in Electronics and Applied Physics, University of Maryland, College Park, Maryland 20742, United States
[d]Department of Materials Science and Engineering, University of Maryland, College Park, Maryland 20742, United States
[e]Sandia National Laboratories, Livermore, California 94551, USA

†Certain commercial equipment, instruments, or materials are identified in this document. Such identification does not imply recommendation or endorsement by the National Institute of Standards and Technology, nor does it imply that the products identified are necessarily the best available for the purpose.

1 Chan, C.K., Peng, H., Liu, G., McLwrath, K., Zhang, X. F., Huggins, R.A., Cui, Y. *Nature Nanotechnol.*, 2008, **3**, 31-35.

2 Song, M.-K., Park, S., Alamgir, F. M., Cho, J., Liu, M. *Mat. Sci. Eng.*, 2011, *R* **72**, 203-252.

3 Lee, S.W., McDowell, M.T., Berla, L.A., Nix, W.D., Cui, Y. *Proc. Nat. Acad. Sci.*, 2012, **109,** 4080-4085.

4 Lee, B.-S., Son, S.-B., Park, K.-M., Seo, J.-H., Lee, S.H., Choi I.-S., Oh, K.-H., Yu, W.-R. *J. Power Sources*, 2012, **206**, 267-273.

5 P.G. Bruce, S.A. Freunberger, L.J. Hardwick, J.-M. Tarascon, *Nature Mater.*, 2012, **11**, 19-29.

6 Vullers, R.J.M., Van Schaijk, R., Doms, I., Van Hoof, C., Mertens, R. *Solid-State Electronics*, 2009, **53**, 684–693.

7 B. Dunn, J.W. Long, D.R. Rolison, *The Electrochemical Society Interface*, 2008, **17**, 49-53.

8 D.R. Rolison, L.F. Nazar, *MRS Bull.* 2011, **36**, 486- 492.

9 Oudenhoven, J. F. M., Baggetto, L., Notten, P. H. L., *Adv. Energy Mater.*, 2011, **1**, 10–33

10 Shao-Horn, Y., Croguennec, L., Delmas, C., Nelson, E.C., O'Keefe, M. *Nature Mater.*, 2003, **2**, 464-467.

11 A. Brazier, L. Dupont, L. Dantras-Laffont, N. Kuwata, J. Kawamura, J.-M. Tarascon, *Chem. Mater.*, 2008, **20**, 2352–2359.

12 Oleshko, V.P., Scordilis-Kelley, C., Xiao, A., Affinito, J., Talyossef, Y., Elazari, R., Grinblat, Y., Aurbach, D., *Microsc. Microanal.*, 2009, **15** (Suppl. 2), 1398-1399.

13 Muto, S., Yoshida, T., Tatsumi, K. *Mater. Trans.*,2009, **50**, 964-969.

14 Muto, S., Tatsumi, K., Sasaki, T., Kondo, H., Ohsuna, T., Horibuchi, K., Takeuchi, Y. *Electrochem. Solid-State Lett.*,2010, **13,** A115-A117.

15 Yamamoto, K., Iriyama,Y., Asaka, T., Hirayama, T., Fujita, H., Fisher, C. A. J., Nonaka, K., Sugita, Y., Ogumi, Z. *Angew. Chem. Int. Ed.*, 2010, **49**, 4414 –4417.

16 Jarvis, K. A., Deng, Z., Allard, L.F., Manthiram, A., Ferreira, P.J. *Chem. Mater.*, 2011, **23**, 3614-3621.

17 Huang, R., Hitosugi, T., Findlay, S.D., Fisher, C.A.J., Ikuhara, Y. H. *Appl. Phys. Lett.*, 2011, **98**, 051913.

18 Oleshko, V., Ruzmetov, D., Lezec, H., Talin, A. *Microsc. Microanal.*, 2011, **17** (Suppl. 2), 1658-1659.

19 Oleshko, V.P., Ruzmetov, D., Haney, P., Lezec, H., Karki, K., Baloch, K.H., Agrawal, A., Davydov, A.V., Krylyuk, S., Moon, K.W., Bonevich, J., Tanase, M., Cumings, J., Talin, A.A. *Microsc. Microanal.*, 2012, **18** (Suppl. 2), 1322-1323.

20 Cosandey, F., Su, D., Sina, M., Pereira, N., Amatucci, G. G *Micron*, 2012, **43**, 22-29.

21 Oleshko, V.P., Scordilis-Kelley, C., Xiao, A. *Microsc. Microanal.*, 2009, **15** (Suppl. 2), 718-719.

22 Huang, J.Y., Zhong, L., Wang, C.M., Sullivan, J. P., Xu, W., Zhang L., Q., Mao, S. X., Hudak, N.S., Liu, X. H., Subramanian, A., Fan, H. Qi, L., Kushima, A., Li J. *Science*, 2010, **330,** 1515-1520.

23 Unocic, R.R., Adamczyk, L.A., Dudney, N.J., Alsem, D.H., Salmon N.J., More, K.L., *Microsc. Microanal.*, 2011, **17** (Suppl 2), 1564-1565.

24 Jungjohann, K.L., Evans, J.E., Aguiar, J.A. Arslan, I., Browning N.D. *Microsc. Microanal.*, 2012, **18**, 621–627.

25 Sullivan, J.P., Huang, J., Shaw, M.J., Subramanian, A., Hudak, N., Zhan, Y., Lou, J., in: *Energy Harvesting and Storage: Materials, Devices, and Applications, eds. Dhar, N.K., Wijewarnasuriya, P.S., Dutta, A.K. Proc. SPIE*, 2010, **7683**, 76830B 1-9.

26 Wang, C.M., Xu, W., Liu, J., Choi, D.W., Arey, B., Saraf, L.V., Zhang, J.G., Yang, Z.G., Thevuthasan, S., Baer, D.R., Salmon, N. *J. Mater. Res.*, 2010, **25**(8), 1541-1547.

27 Wang, C.M., Li, X., Wang, Z., Xu, W., Liu, J., Gao, F., Kovarik, L., Zhang, J.-G., Howe, J., Burton, D.J., Liu, Z., Xiao, X., Thevuthasan, S., Baer, D.R. *Nano Lett.*, 2012, **12**, 1624−1632.

28 Liu, X. H., Zhong, L., Zhang, L.Q., Kushima, A., Mao, S. X., Li, J., Ye, Z. Z., Sullivan, J.P., Huang, J.Y. *Appl. Phys. Lett.*, 2011, **98**, 183107.

29 Liu, X.H., Zheng, H., Zhong, L., Huang, S., Karki, K., Zhang, L.Q., Liu, Y., Kushima, A., Liang, W.T., Wang, J.W., Cho, J-H., Epstein, E., Dayeh, S.A., Picraux, S.T., Zhu, T., Li, J., Sullivan, J.P., Cumings, J., Wang, C., Mao, S.X., Ye, Z.Z., Zhang, S., Huang, J.Y. *Nano Lett.*, 2011, **11**, 3312-3318.

30 Liu, X.H., Hudak, N.S., Huber, D.L., Limmer, S.J., Sullivan, J.P., Huang, J.Y. *Nano Lett.*, 2011, **11**, 4188-4194.

31 Karki, K., Epstein, E., Cho, J.-H., Jia, Z., Li, T., Picraux, S. T., Wang, C., Cumings, J. *Nano Lett.*, 2012, **12**, 1392-1397.

32 Meng, Y. S., McGilvray, T., Yang, M.-C., Gostovic, D., Wang, F., Zeng, D., Zhu, Y., Graetz J. *The Electrochemical Society Interface*, 2011, **130**(3), 49-53.

33 Mai, L., Dong, Y., Xu, L., Han, C. *Nano Lett*., 2010, **10**, 4273–4278.

34 Yu, X., Bates, J.B., Jellison, G.E., Hart, F.X. *J. Electrochem. Soc.*, 1997, **144,** 524-532.

35 J.B. Bates, N.J. Dudney, B. Neudecker, F.X. Hart, H.P. Jun, S.A. Hackney, *J. Electrochem. Soc.*, 2000, **147,** 59-70.

36 J.B. Bates, N.J. Dudney, B. Neudecker, A. Ueda, C.D. Evans, *Solid State Ionics*, 2000, **135**, 33-45.

37 Ruzmetov, D., Oleshko, V.P., Haney, P.M., Lezec, H., Karki, K., Baloch, K.H., Agrawal, A.K., Davydov, A.V., Krylyuk, S., Liu, Y., Huang, J.Y., Tanase, M., Cumings J., Talin, A.A. *Nano Lett*., 2012, **12**, 505-511.

38 Chan, C.K., Patel, R.N., O'Connel, M.J., Korgel, B.A., Cui, Y. *ACS Nano, 2010*, **4**, 1443-1450.

39 Cui, L.F., Ruffo, R., Chan, C.K., Peng, H., Cui, Y. *Nano Lett.*, 2009, **9**, 491-495.

40 Krylyuk, S., Davydov, A.V., Levin I. *ACS Nano*, 2011, **5**, 656 – 664.

41 N.D. Browning, I. Arslan, R. Erni, B.W. Reed, in: *Scanning Transmission Electron Microscopy. Imaging and Analysis*. Eds. Pennycook, S.J., Nellist, P.D., New York: Springer, 2011, 659-688.

42 Reed, B.W., Chen, J.M., MacDonald, N.C., Silcox, J., Bertsch, G.F. *Phys. Rev. B*, 1999, **60**, 5641-5652.

43 Moreau P., Brun, N., Walsh, C.A., Colliex, C., Howie, A. *Phys. Rev. B*, 1997, **56**, 6774-6781.

44 H. Ibach, J.E. Rowe, *Phys. Rev. B*, 1974, **10**, 710-718.

45 S.J. Pennycook, in: *Scanning Transmission Electron Microscopy. Imaging and Analysis*. Eds. S.J. Pennycook, P.D. Nellist, New York: 2011, Springer, 1-90.

46 P.D. Nellist, in: *Scanning Transmission Electron Microscopy. Imaging and Analysis*. Eds. S.J. Pennycook, P.D. Nellist, New York: Springer, 2011, 91-115.

47 S. Bals, B. Kabius, M. Haider, V. Radmilovic, C. Kisielevski, *Solid State Comm.* 2004. **130**, 675-680.

48 C. Jeanguillaume, *J. Microsc. Electron.*, 1985, **10**, 409-415.

49 N. Bonnet, M. Herbin, P. Vaurot, *Scan. Microsc.* 1997, **11**, 1-21.

50 Grogger, W., Hofer, F., Kothleitner G. *Micron*, 1998, **29**, 43-51.

51 Sarahan, M.C., Chi, M., Masief, D.J., Browning, N.D. *Ultramicroscopy*, 2011, **111**, 251-257.

52 L. Bohne, T. Pirk, W. Jaegermann, *J. Solid State Electrochem.* 2011, 1377-9.

53 Xie, J., Imanishi, N., Hirano, A., Matsumura, M., Takeda, Y., Yamamoto, O., *Solid State Ionics*, 2007, **178**, 1218–1224

54 Kim, Y., Veigth, G.M., Nanda, J., Unocic, R.R., Chi, M., Dudney, N.J. *Electrochim. Acta*, 2011, **56,** 6573-6580.

55 Song, S.-W., Baek, S.-W., Park, H.Y., Lim, Y.C., Lee, K.L. *Electrochem. Solid-State Lett*., 2008, **11**, A55-A59.

56 Huang, R., Hitosugi, T., Fisher, C.A.J., Ikuhara, Y.H. Moriwake, H., Oki, H., Ikuhara, Y. *Mater. Chem. Phys.*, 2012, **133**, 1101-1107.

57 Okubo, M., Kim, J., Kudo, T., Zhou, H., Honma, I., *J. Phys. Chem*., 2009, **113**, 15337-15342.

58 Danilov, D., Niessen, R.A.H., Notten, P.H.L. *J. Electrochem. Soc*., 2011, **158**, A215-A222.

59 Reimers, J. N., Dahn, J. R. *J. Electrochem. Soc.*, 1992, **139** , 2091-2097.

60 Wang, H., Jang, Y., Huang, B., Sadoway, D.R., Chiang, Y.-M. *Electrochem Soc.*, 1999, **146,** 473-480**.**

61 M.A. Lampert, P. Mark, *Current Injection in Solids*, New York: Academic Press, 1970.